Neutron scattering study of the orientational disorder and phase transitions in barium carbonate

Guanqun Cai[1], Anthony E Phillips[1], Matthew G Tucker[2], Martin T Dove[3,4]

[1] School of Physics and Astronomy, Queen Mary University of London, Mile End Road, London, E1 4NS, U.K.

[2]Oak Ridge National Laboratory, Neutron Scattering Division, 1 Bethel Valley Road, Oak Ridge, TN 37831, USA

[3]Department of Physics, School of Sciences, Wuhan University of Technology, 205 Luoshi Road, Hongshan district, Wuhan, Hubei, 430070, People's Republic of China

[4]College of Computer Science and College of Physical Science & Technology, Sichuan University, Chengdu 610065, People's Republic of China

E-mail: martin.dove@icloud.com

Abstract. Orientational disorder of the molecular CO_3^{2-} anions in $BaCO_3$, which occurs naturally as the mineral witherite, has been studied using a combination of neutron total scattering analysed by the Reverse Monte Carlo method and molecular dynamics simulations. The primary focus is on the phase transition to the cubic phase, which assumes a rocksalt structure (Strukturbericht type B1) with highly disordered orientations consistent with the mismatch between the site ($m\overline{3}m$) and molecular ($3/m$) symmetries. Both experiment and simulation show a high degree of disorder, with the C–O bond orientation distribution never exceeding 25% variation from that of a completely uniform distribution, although there are differences between the two methods regarding the nature of these variations. Molecular dynamics simulations are also reported for the analogous phase transitions in the very important mineral calcite, $CaCO_3$. The combination of the simulations and comparison with $BaCO_3$ shows that the properties of calcite at all temperatures within its stability field are affected mostly by the onset of orientational disorder associated with the high-temperature cubic phase, even though this lies outside the stability field of calcite. This is a new understanding of calcite, which previously had been interpreted purely in terms of the phase transition to an intermediate partially-disordered phase. Finally, we also found that witherite itself appears to support the development of orientational disorder on heating, with the simulations showing a sequence of phase transitions that explain the much larger thermal expansion of one axis.

1. Introduction

Calcium carbonate, $CaCO_3$, is the most significant of the non-silicate minerals found in the Earth's crust, forming as chalk, limestone and marble, and playing an important role in both the water and carbon dioxide budgets of the planet. Calcite is well-known in the

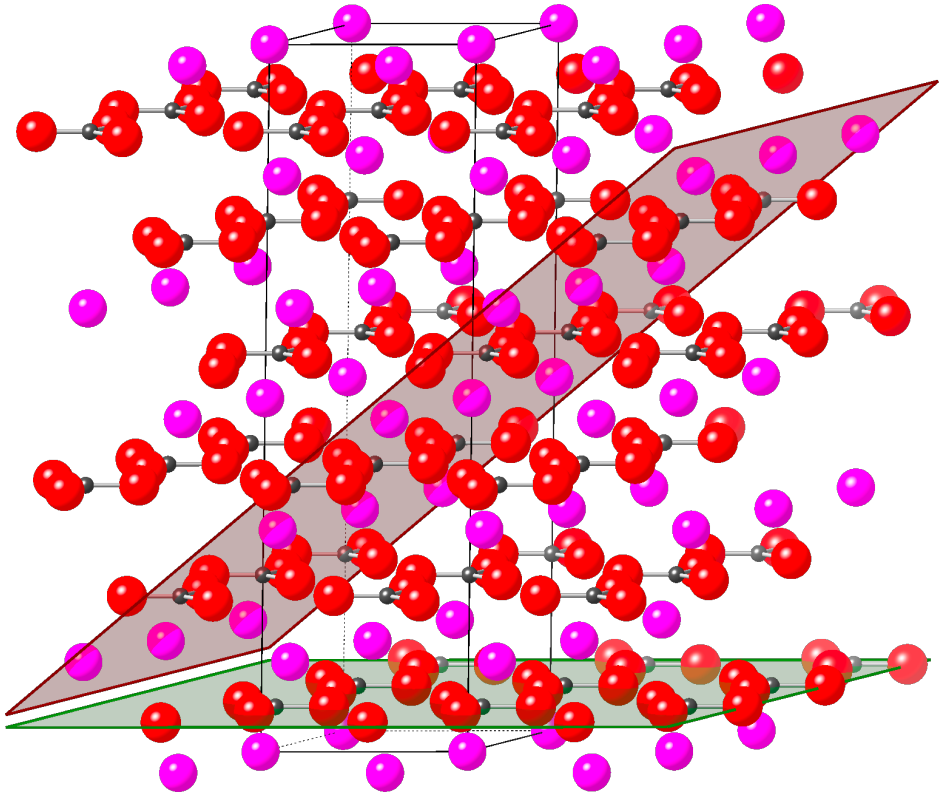

Figure 1: Crystal structure of the $R\bar{3}c$ phase of calcite, $CaCO_3$. The CO_3 groups (carbon atoms as gray spheres, oxygen atoms as red spheres) lie in planes parallel to the trigonal (0001) plane, separated by layers of calcium atoms (pink spheres). One (0001) plane (translucent green) is shown to highlight the flat layers of carbonate molecular anions. The figure also shows the electrically neutral $(10\bar{1}4)$ planes which form the predominant crystal habit (translucent red).

form of Iceland Spar, where the beautiful single crystals with well-defined habit show the dramatic effect of double refraction. The characteristic shape of crystals of Iceland Spar comes from the set of $(10\bar{1}4)$ planes‡ that form the crystal faces, as shown in Figure 1, because these are the electrically neutral planes in the crystal §. Calcite actually has a rather unusual thermal expansion, with a relatively large (for a mineral) positive linear expansivity along the trigonal [001] direction and small but negative linear expansivity along the perpendicular directions [1, 2].

The large positive expansivity along the trigonal [001] direction has been associated with a probable orientational order–disorder phase transition at high temperature [3, 4]. The Bragg reflections of the room-temperature phase where the Miller indices $(hki\ell)$ have odd values of ℓ fall to zero on heating towards a temperature of around 1260 K [3, 4]. This is consistent with a phase transition from the room temperature structure of space group

‡ We use the four-index notation for the rhombohedral phases described in the hexagonal/trigonal system.

§ That is, there is no surface dipole moment.

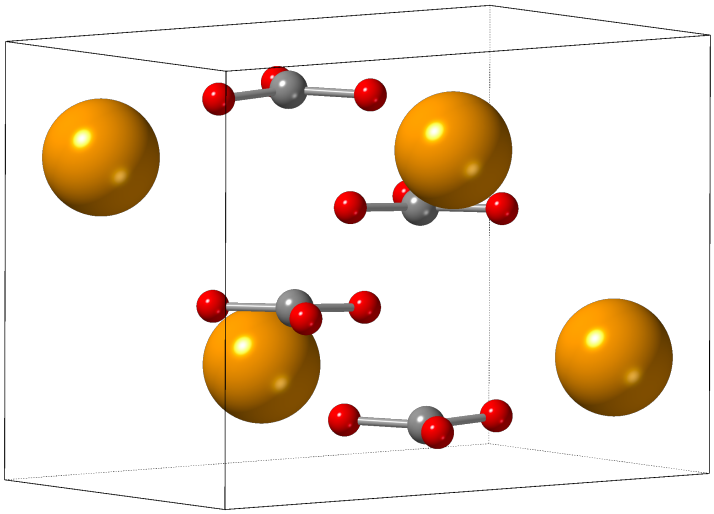

Figure 2: Crystal structure of the orthorhombic *Pmcn* phase of witherite, $BaCO_3$ [5, 6, 7, 8]. The CO_3 groups (carbon atoms as gray spheres, oxygen atoms as red spheres) lie in planes parallel to the orthorhombic (001) plane, separated by layers of barium atoms (gold spheres).

$R\bar{3}c$ to that of space group $R\bar{3}m$ with a halving of the trigonal c lattice parameter. Such a transition could be achieved if the carbonate groups become orientationally disordered about axes parallel to the trigonal [001] direction. This aspect was studied by neutron powder diffraction [4], showing two interesting unexpected effects. The first was that on heating the carbonate molecular anions show a large increase in librational amplitude and no growth in the number of anions with a 60° rotation, and secondly a large increase in the amplitude of libration about axes perpendicular to the molecular 3-fold axis. This increase in the perpendicular libration was suggested to explain the rather large thermal expansion of the c axis that appeared to be associated with the phase transition.

Experimentally this was as far as was possible to get to, because the carbonate molecular anions become chemically unstable at the point of the $R\bar{3}c$–$R\bar{3}m$ phase transition, with the rapid decomposition reaction $CaCO_3 \rightarrow CaO + CO_2$. Attempts to prevent this reaction, or at least raise it to a higher temperature, through the use of a pressurised CO_2 environment were unsuccessful [4]. This means that the true nature of the $R\bar{3}m$ phase and hence of the phase transition cannot be confirmed, and neither can we establish a baseline thermal expansion for the $R\bar{3}m$ phase with which to confirm that the origin of the thermal expansion of the $R\bar{3}c$ phase is associated solely with this phase transition.

Subsequent molecular dynamics simulations, which we report here, suggest that the $R\bar{3}c$–$R\bar{3}m$ phase transition is part of a larger sequence of phase transitions that ultimately reach an orientationally disordered phase with the simple cubic rocksalt structure. Indeed, it is almost a textbook observation that the C and Ca ions in calcite have a distorted rocksalt arrangement.

Although we cannot access this state in calcite, it appears that a similar

orientationally-disordered rocksalt phase exists in $BaCO_3$ [9]. Actually at ambient conditions $BaCO_3$ is found as the mineral witherite [5, 6, 7, 8], which has the aragonite structure adopted by $CaCO_3$, as shown in Figure 2 (orthorhombic symmetry, space group $Pmcn$; details of the crystal structure will be reported below) at a slight high pressure. At a temperature of 1084 K [6] it transforms to a rhombohedral phase of symmetry either $R3m$ or $R\bar{3}m$; the former is ordered with all carbonate anions the same orientation, and the latter is necessarily disordered with respect to the orientations of the carbonate anions. Subsequently at a temperature of 1255 K [6] it transforms to the disordered rocksalt cubic phase [9], until eventually undergoing the decomposition reaction $BaCO_3 \rightarrow BaO + CO_2$.

In this paper we use the method of neutron total scattering coupled with the Reverse Monte Carlo method to investigate the atomic structure of the orientationally disordered cubic phase of $BaCO_3$. We also report supporting molecular dynamics simulations to provide the wider context and to give a point of comparison. It is to be hoped that as a result of this work we will have a much better understanding of the properties experienced at ambient conditions by the important life-giving mineral calcite.

2. Methods

2.1. Molecular dynamics simulations

Molecular dynamics (MD) simulations were performed using the `DL_POLY` code [10]. The potential energy function of Archer et al [11] was used with rigid CO_3 molecules and rigid ions. This was chosen in preference to other alternatives in the literature [12] because it was been specifically tuned to account for the vibrational dynamics of calcite, and in particular to reproduce the soft phonon branch associated with the high-pressure phase transition, whilst retaining full stability, and it was designed to allow for a wide range of divalent cations.

Simulation boxes with orthogonal axes of approximate length 50 Å were prepared using the `data2config/rmcreate` program [13]. One axis is along the trigonal [001] axis, one along the trigonal [100] axis, and the third along the orthogonal [210] axis. MD simulations were also performed using configurations from the witherite crystal structure.

In all cases we used time steps of 0.005 ps. Simulations were equilibrated for 10,000 steps (50 ps) and run for 50,000 steps (250 ps) to generate configurations for analysis. We used constant-stress [14, 15] and constant temperature [16, 17] thermodynamic ensembles.

2.2. Neutron powder diffraction and total scattering measurements

For the experimental work reported here $BaCO_3$ was obtained commercially. A sample was loaded into a thin-walled vanadium can, which was itself placed into a vacuum furnace. Neutron scattering measurements were performed on the GEM instrument at the ISIS spallation neutron facility [18]. Long measurements were performed for total

scattering analysis, with shorter measurements for Rietveld analysis. For data correction, measurements were also made of the empty instrument, empty furnace, and empty sample can within the furnace, together with a calibration measurement of a vanadium rod.

The data were prepared in a form for Rietveld refinement using the MANTID software [19]. The total scattering data were corrected using the GUDRUN code [20]. The end result was the scattering function $i(Q)$,

$$i(Q) = 4\pi\rho \int \sum_{m,n} c_m c_n b_m b_n r^2 \left(g_{mn}(r) - 1\right) \frac{\sin(Qr)}{Qr} \, \mathrm{d}r \tag{1}$$

where Q is the modulus of the scattering vector, and the Fourier transform of $i(Q)$, the pair distribution function (PDF), has the form

$$D(r) = \frac{2}{\pi} \int_0^\infty Q i(Q) \sin(Qr) \, \mathrm{d}r = 4\pi\rho r \sum_{m,n} c_m c_n b_m b_n \left(g_{mn}(r) - 1\right) \tag{2}$$

In these equations the partial function $g_{mn}(r)$ is defined such that the number of atoms of type n lying within a spherical shell of thickness $\mathrm{d}r$ at a distance r from an atom of type m is given as $4\pi r^2 \mathrm{d}r \times c_n\rho \times g_{mn}(r)$. The function $g_{mn}(r)$ is effectively a multiplicative factor that determines how much the distribution of atoms of type n differs from random at specific distances from atoms of type m; it has a value equal to 1 when the distribution at a distance of r gives the same density within the spherical shell as that for a random distribution. ρ is the atomic number density. The other quantities are c_m to represent the fractional concentration of atoms of type m, and b_m as the coherent scattering length of atom of type m. Further discussion of these functions, and comparisons with other functions in common use, has been given by Keen [21].

2.3. Rietveld analysis

The Rietveld refinements of the different structures of $BaCO_3$ were performed using the GSAS/EXPGUI [22, 23] and GSAS II [24] programs. A representative fit for the ordered witherite phase is shown in Figure 3. Results for lattice parameters are given in Table 1, for atomic fractional coordinates in Table 2, and for atomic displacement parameters in Tables 3 and 4. The table reports refinements in two different space groups for the intermediate temperature phase; we found that both gave equivalent quality fits for data from all neutron banks except the highest-resolution bank of angle 154.40°. As shown in Figure 4, the $R\bar{3}m$ model gives a better fit and correct relative peak heights. Table 4 shows the model refined with $R3m$ space group has a large Ba atomic displacement parameter, which is comparable with the C atomic displacement parameter. However, in the witherite phase and the cubic phase, the heavy atom Ba always has a much smaller atomic displacement parameter than the light atom C. Meanwhile, the $R\bar{3}m$ models have atomic displacement parameters more consistent with other phases. Therefore, we believe $R\bar{3}m$ is more likely to be the space group of the intermediate-temperature phase, in spite of the discussion given by Antao and Hassan [6].

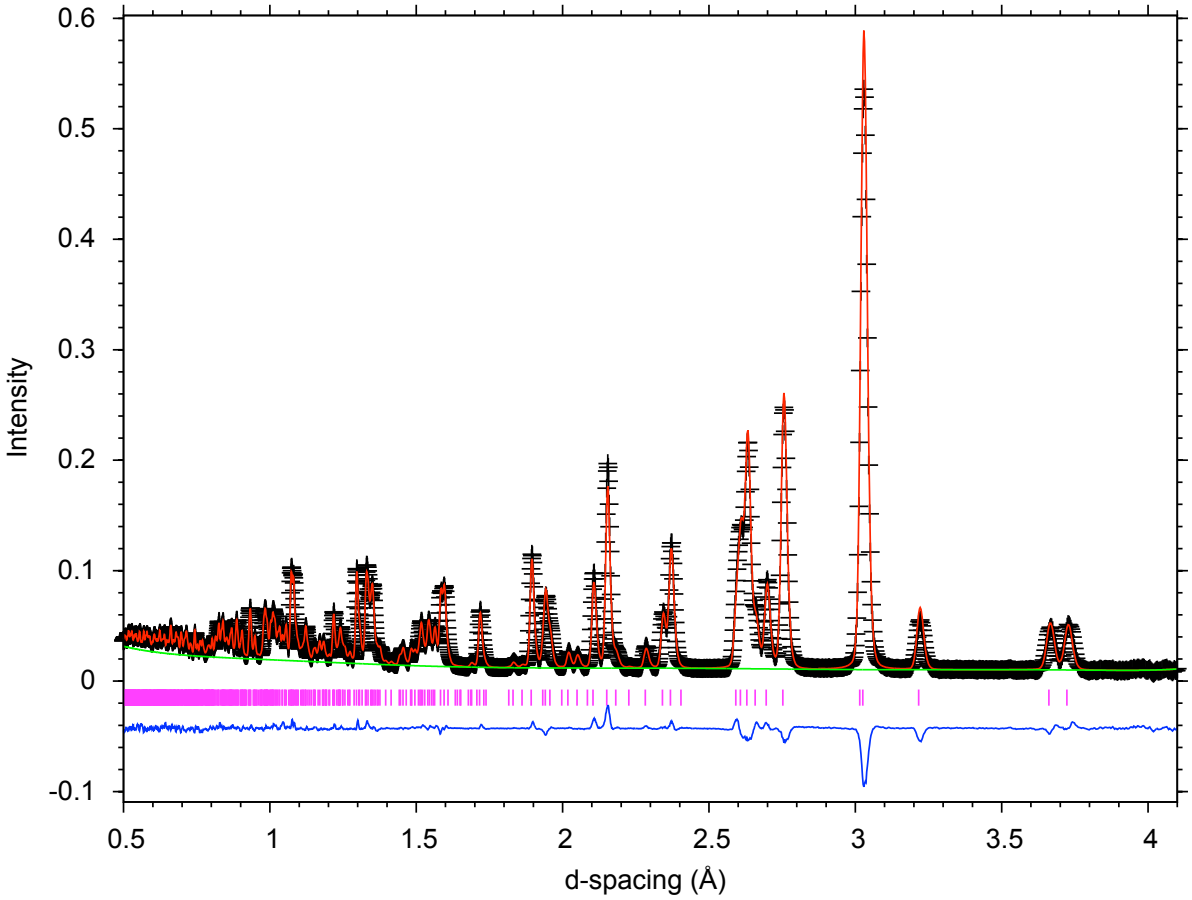

Figure 3: A representative fit of diffraction data using Rietveld refinement, shown for the witherite phase at a temperature of 25 °C, with data from the detector bank of nominal scattering angle 63.42°. The black crosses are the data and the red curve is the fitted diffraction profile. The green line indicates the fitted background, and the blue curve represents the difference between data and fitted profile. The magenta vertical lines represent the positions of the Bragg peaks.

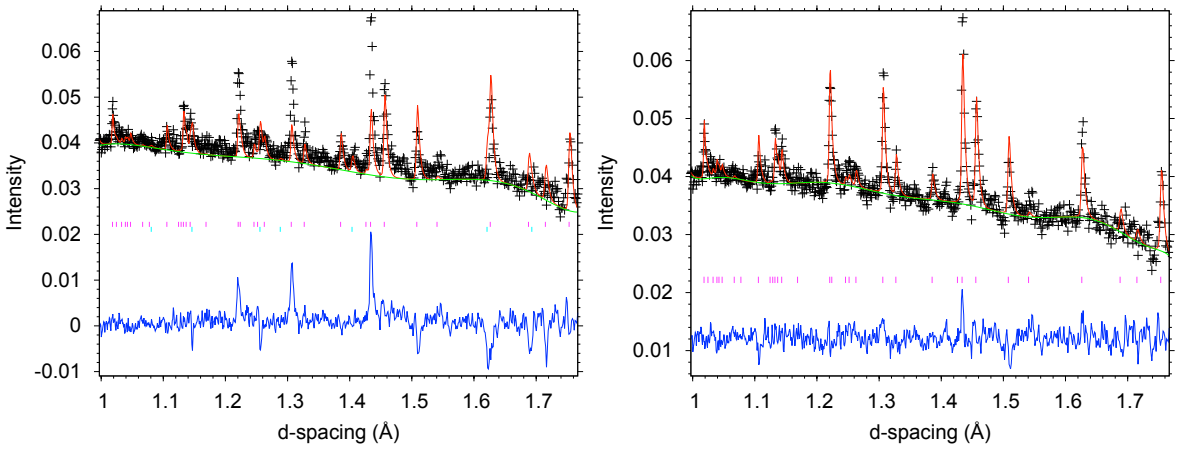

(a) $R3m$ (b) $R\bar{3}m$

Figure 4: Comparison of the fits to the highest-resolution diffraction data (detector bank of nominal scattering angle 154.40°) obtained for a temperature of 850 °C from Rietveld refinement, using the crystal structures of the two candidate rhombohedral phases of symmetry $R3m$ and $R\bar{3}m$. The black crosses are the data, the red curves are the fitted diffraction profiles, the green lines indicate the fitted backgrounds, and the blue curves represent the difference between data and fitted profile. The magenta vertical lines represent the positions of the Bragg peaks. A better agreement was obtained with the disordered $R\bar{3}m$ structure.

Table 1: Lattice parameter data for the three phases of $BaCO_3$. These results were obtained by Rietveld refinement of the diffraction data from the GEM diffractometer at ISIS. Horizontal lines demarcate different phases; the top group is for the phase with space group symmetry $Pmcn$, the middle group is for rhombohedral symmetry of either $R\bar{3}m$ or $R3m$, and the bottom line is for cubic space group $Fm\bar{3}m$. Here and in Tables 2–4 we give the temperatures in the units for the measurement, namely °C, but in the main text we will refer to temperatures in units of K for direct comarison with the molecular dynamics simulations.

T (°C)	a (Å)	b (Å)	c (Å)
25	5.3305(25)	8.9288(4)	6.45167(19)
25	5.3282(26)	8.9250(5)	6.44887(20)
100	5.31743(6)	8.90467(11)	6.45480(7)
150	5.31915(6)	8.90636(11)	6.46966(7)
200	5.32087(5)	8.90804(9)	6.48472(6)
250	5.32259(7)	8.90963(12	6.49905(7)
300	5.32424(7)	8.91161(12)	6.51668(8)
350	5.32694(9)	8.91577(16)	6.53620(8)
400	5.32873(10)	8.91751(17)	6.55370(8)
450	5.33042(10)	8.92006(18)	6.57253(9)
500	5.33176(11)	8.92226(20)	6.59073(10)
550	5.33360(13)	8.92580(23)	6.61110(11)
650	5.33955(14)	8.93600(26)	6.65945(12)
700	5.34124(15)	8.94086(28)	6.68444(13)
750	5.34276(17)	8.94649(32)	6.71179(16)
800	5.34375(18)	8.9535(4)	6.74229(18)
850	5.22387(12)	—	10.5688(10)
900	5.20132(11)	—	10.65650(26)
950	5.16208(11)	—	10.87436(30)
850	5.22399(9)	—	10.51903(22)
900	5.20137(9)	—	10.65672(21)
950	5.16216(10)	—	10.87424(27)
1000	6.9712(2)	—	—

Table 2: Atomic fractional coordinates for the various phases of $BaCO_3$ as indicated in the table. In the space group $Pmcm$ by symmetry $x = 1/4$ for Ba, C and O1. In the $R3m$ phase $x = y = 0$ for Ba and C, and $y = -x$ for O. In the $R\bar{3}m$ phase Ba has $x = y = 0$ and $z = \frac{1}{4}$, C has $x = y = z = 0$ and O has $y = z = 0$. In the cubic $Fm\bar{3}m$ phase Ba has coordinates $(0, 0, \frac{1}{2})$, C has coordinates $(0, 0, 0)$, and O has $x = 0$ and $y = -z$. These results were obtained by Rietveld refinement of the diffraction data from the GEM diffractometer at ISIS.

$Pmcn$	T (°C)	Ba y	Ba z	C y	C z	O1 y	O1 z	O2 x	O2 y	O2 z
	25	0.4164(3)	0.7538(5)	0.7567(3)	−0.0810(4)	0.9015(3)	−0.0894(5)	0.4598(3)	0.6831(2)	−0.0806(4)
	25	0.4165(4)	0.7537(5)	0.7568(3)	−0.0808(4)	0.9017(3)	−0.0897(6)	0.4598(3)	0.6832(2)	−0.0808(4)
	100	0.4168(1)	0.7542(2)	0.7570(1)	−0.0810(2)	0.9011(1)	−0.0878(2)	0.4595(1)	0.6839(1)	−0.0790(2)
	150	0.4166(1)	0.7543(2)	0.7570(1)	−0.0810(2)	0.9011(1)	−0.0878(2)	0.4594(1)	0.6839(1)	−0.0790(2)
	200	0.4166(1)	0.7541(2)	0.7570(1)	−0.0810(1)	0.9011(1)	−0.0878(2)	0.4594(1)	0.6839(1)	−0.0790(1)
	250	0.4165(2)	0.7539(2)	0.7570(1)	−0.0810(2)	0.9010(1)	−0.0877(3)	0.4593(1)	0.6840(1)	−0.0790(2)
	300	0.4167(2)	0.7540(2)	0.7570(1)	−0.0810(2)	0.9010(1)	−0.0877(3)	0.4593(1)	0.6840(1)	−0.0790(2)
	350	0.4164(2)	0.7549(2)	0.7571(1)	−0.0770(2)	0.9000(2)	−0.0860(3)	0.4583(2)	0.6840(1)	−0.0772(2)
	400	0.4167(2)	0.7548(3)	0.7573(2)	−0.0765(2)	0.8998(2)	−0.0850(3)	0.4589(2)	0.6844(1)	−0.0767(2)
	450	0.4160(2)	0.7560(3)	0.7571(2)	−0.0748(3)	0.8999(2)	−0.0839(3)	0.4590(2)	0.6853(1)	−0.0759(2)
	500	0.4161(2)	0.7560(3)	0.7568(2)	−0.0740(3)	0.9004(2)	−0.0841(4)	0.4589(2)	0.6858(1)	−0.0751(2)
	550	0.4163(3)	0.7561(3)	0.7575(3)	−0.0722(3)	0.9003(3)	−0.0843(4)	0.4587(2)	0.6867(2)	−0.0738(3)
	650	0.4166(3)	0.7569(4)	0.7579(3)	−0.0710(4)	0.8994(3)	−0.0837(4)	0.4555(3)	0.6858(2)	−0.0732(3)
	700	0.4164(3)	0.7581(4)	0.7575(3)	−0.0694(4)	0.8998(4)	−0.0810(5)	0.4554(3)	0.6868(2)	−0.0731(3)
	750	0.4157(4)	0.7572(4)	0.7583(3)	−0.0682(5)	0.9010(4)	−0.0795(5)	0.4548(4)	0.6881(2)	−0.0717(4)
	800	0.4173(4)	0.7637(4)	0.7573(4)	−0.0601(6)	0.8970(4)	−0.0816(6)	0.4555(4)	0.6881(3)	−0.0718(4)
$R3m$	T (°C)	Ba z	C z	O x	O z					
	850	0.1257(6)	0.6012(6)	0.136(4)	0.6012(6)					
	900	0.0840(9)	0.5664(7)	0.140(5)	0.5664(7)					
	950	0.0795(8)	0.5681(9)	0.1124(3)	0.5637(9)					
$R\bar{3}m$	T (°C)	O x								
	850	0.2106(7)								
	900	0.2109(8)								
	950	0.2055(10)								
$Fm\bar{3}m$	T (°C)	O z								
	1000	0.1132(4)								

Table 3: Atomic displacement parameters for the witherite phase of $BaCO_3$. These results were obtained by Rietveld refinement of the diffraction data from the GEM diffractometer at ISIS.

T (°C)	Ba U_{iso}	C U_{iso}	O U_{11}	O U_{12}	O U_{13}	O U_{22}	O U_{23}	O U_{33}
25	0.00425(17)	0.00720(16)	0.0035(4)	—	—	0.0021(4)	-0.0036(5)	0.0296(6)
			0.00163(25)	0.00210(24)	-0.00314(34)	0.00414(26)	0.0040(4)	0.0329(4)
25	0.00404(19)	0.00729(17)	0.0031(5)	—	—	0.0023(4)	-0.0032(5)	0.0290(7)
			0.00146(27)	0.00178(26)	-0.0034(4)	0.00387(29)	0.0044(4)	0.0334(5)
100	0.00547(22)	0.00906(20)	0.0069(6)	—	—	0.0030(5)	-0.0035(6)	0.0349(8)
			0.00238(33)	0.00282(31)	-0.0039(4)	0.00642(35)	0.0048(5)	0.0423(6)
150	0.00654(24)	0.01060(22)	0.0078(7)	—	—	0.0039(5)	-0.0019(7)	0.0386(9)
			0.00303(35)	0.00248(33)	-0.0030(5)	0.0080(4)	0.0063(6)	0.0473(6)
200	0.0076(7)	0.0115(6)	0.0098(6)	—	—	0.0050(5)	-0.0025(6)	0.0432(8)
			0.00389(31)	0.00348(29)	-0.0037(4)	0.00946(33)	0.0053(5)	0.0514(6)
250	0.00855(27)	0.01281(24)	0.0120(8)	—	—	0.0061(6)	-0.0016(8)	0.0474(10)
			0.0046(4)	0.0040(4)	-0.0045(5)	0.0112(4)	0.0046(6)	0.0573(7)
300	0.01007(29)	0.01430(26)	0.0157(9)	—	—	0.0073(7)	-0.0039(8)	0.0512(11)
			0.0051(5)	0.0039(4)	-0.0043(6)	0.0140(5)	0.0057(7)	0.0634(8)
350	0.00965(31)	0.01802(31)	0.0126(13)	—	—	0.0104(9)	0.0006(11)	0.0660(14)
			0.0071(7)	0.0016(5)	-0.0035(8)	0.0134(6)	0.0048(8)	0.0665(10)
400	0.00923(34)	0.01704(32)	0.0172(14)	—	—	0.0117(10)	-0.0001(12)	0.0657(15)
			0.0057(7)	0.0022(6)	-0.0041(8)	0.0136(6)	0.0031(9)	0.0702(10)
450	0.00822(34)	0.01747(35)	0.0200(15)	—	—	0.0132(10)	0.0036(13)	0.0699(16)
			0.0070(8)	0.0037(6)	-0.0017(9)	0.0134(7)	-0.0003(10)	0.0743(11)
500	0.00646(34)	0.0167(4)	0.0209(15)	—	—	0.0155(12)	0.0060(14)	0.0733(17)
			0.0060(8)	0.0045(6)	-0.0014(10)	0.0157(7)	-0.0044(11)	0.0795(12)
550	0.0061(4)	0.0172(4)	0.0225(17)	—	—	0.0136(13)	0.0127(16)	0.0763(20)
			0.0069(9)	0.0059(7)	0.0015(11)	0.0158(8)	-0.0078(12)	0.0838(14)
650	0.0125(6)	0.0310(6)	0.0121(20)	—	—	0.0271(17)	0.0062(22)	0.0985(25)
			0.0208(13)	-0.0035(10)	0.0021(14)	0.0213(12)	-0.0013(15)	0.0910(17)
700	0.0100(6)	0.0331(7)	0.0115(20)	—	—	0.0311(19)	0.0074(25)	0.1105(28)
			0.0190(13)	-0.0021(11)	0.0071(14)	0.0251(13)	-0.0030(16)	0.0953(19)
750	0.0073(7)	0.0318(8)	0.0130(23)	—	—	0.0341(21)	0.0123(29)	0.1136(33)
			0.0195(14)	0.0006(12)	0.0118(16)	0.0249(14)	-0.0053(18)	0.1060(22)
800	0.0026(7)	0.0467(11)	-0.0026(22)	—	—	0.0473(28)	0.0722(31)	0.135(4)
			0.0243(16)	0.0036(14)	0.0147(18)	0.0197(16)	-0.0127(19)	0.0936(24)

Table 4: Atomic displacement parameters for the IT and HT phases of $BaCO_3$. These results were obtained by Rietveld refinement of the diffraction data from the GEM diffractometer at ISIS. Horizontal lines demarcate different phases; the top group is for the phase with space group symmetry $R3m$, the middle group is for $R\bar{3}m$ and the bottom line is for cubic space group $Fm\bar{3}m$.

T (°C)	Ba $U_{\rm iso}$	C $U_{\rm iso}$	O U_{11}	O U_{12}	O U_{13}	O U_{22}	O U_{23}	O U_{33}
$R3m$								
850	0.0652(24)	0.0610(18)	0.1484(23)	0.0976(27)	-0.0380(13)	0.1484(23)	0.0380(13)	0.237(4)
900	0.0764(22)	0.0815(23)	0.1481(20)	0.0930(26)	-0.0390(12)	0.1481(20)	0.0390(12)	0.253(4)
950	0.0963(24)	0.1032(27)	0.1581(23)	0.0920(31)	-0.0436(14)	0.1581(23)	0.0436(14)	0.322(6)
$R\bar{3}m$								
850	0.0564(13)	0.0976(18)	0.1190(26)	0.163(6)	0.1021(27)	0.331(11)	0.238(5)	0.3476(34)
900	0.0579(13)	0.1238(23)	0.1232(30)	0.145(7)	0.0934(32)	0.295(13)	0.221(6)	0.3507(34)
950	0.0693(16)	0.155(4)	0.152(4)	0.166(6)	0.1014(32)	0.336(13)	0.237(6)	0.401(4)
$Fm\bar{3}m$								
1000	0.089(5)	0.210(12)	0.411(31)	—	—	0.206(14)	-0.020(10)	0.206(14)

2.4. Reverse Monte Carlo method

The Reverse Monte Carlo method was performed using the `RMCprofile` code [25]. For most of the work we used v6.7, but for the intermediate temperature phase we used a completely new version in prototype form, provisionally assigned version number 7, which is being designed for simulation of more than a single phase ‖. Because of decomposition at high temperature, our first experimental measurements were performed at high temperature, but we lost the first sample due to a malfunction within the furnace. In fact this sample had survived intact on heating into the high-temperature cubic phase with no decomposition detected. The data for the intermediate-temperature phase were obtained on a second sample. Unfortunately, in this case we did see the onset of decomposition, with clear Bragg peaks associated with the presence of BaO. The strategy for the RMC analysis of the intermediate-temperature phase was to use two configurations, alternatively moving one atom at random in each configuration. The relative weights of each phase to the total scattering, PDF [26] and Bragg scattering were determined by the phase fraction determined by the prior Rietveld analysis.

As for the MD simulations, starting configurations of the $BaCO_3$ phases, with orthogonal axes of approximate length 50 Å, were prepared using the `data2config/rmcreate` program [13], using the structures generated by the Rietveld refinement analysis at each temperature and lattice parameters constrained to these values. Minimum distances and interatomic potentials for the C–O bond and O–C–O angles were applied as constraints in the RMC simulations. Taking the RMC simulation of the cubic phase as the example, the minimum allowed distances for the C–C, C–O, C–Ba, O–O, O–Ba and Ba–Ba contacts were 3.8, 1.0, 2.6, 1.93, 2.25 and 3.8 Å respectively. The C–O bond potential was a Morse function with 1.29 Å as the equilibrium distance and 3.5 eV as the difference in energy between the lowest energy and the energy at infinite distance. The O–C–O angle potential was set with 120° as the equilibrium angle and 5.0 eV as the corresponding force constant. Each RMC simulation was run until the average number of successful moves for every atom in the $BaCO_3$ phase was nearly 200, with a maximum single move distance of 0.05 Å.

The BaO configurations used with the multiphase analysis of the intermediate-temperature phase were prepared in the same way and were of similar sizes. BaO has the standard rocksalt structure, space group $Fm\bar{3}m$.

The quality of the RMC fits to data are shown for the example of the witherite phase at room temperature (at this temperature the sample is single phase) in Figure 5. We consider these to be satisfactory. Similar quality was obtained for all temperatures, including for the analyses where we performed two-phase RMC.

‖ This version has not previously been described in the scientific literature, and a paper will be published in due course. Key developers have been Christopher Kerr (University of Cambridge), Wojciech Sławiński (STFC), and the three authors AEP, MGT and MTD.

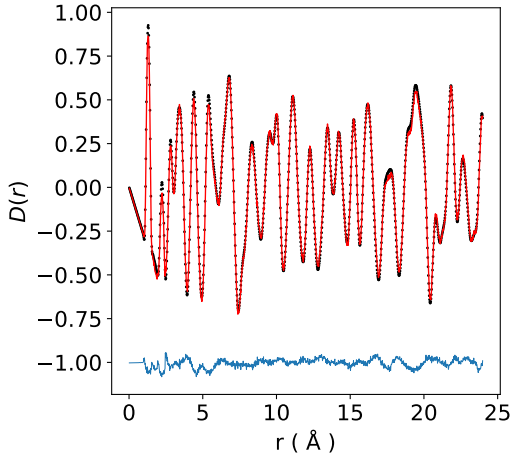

(a) $D(r)$

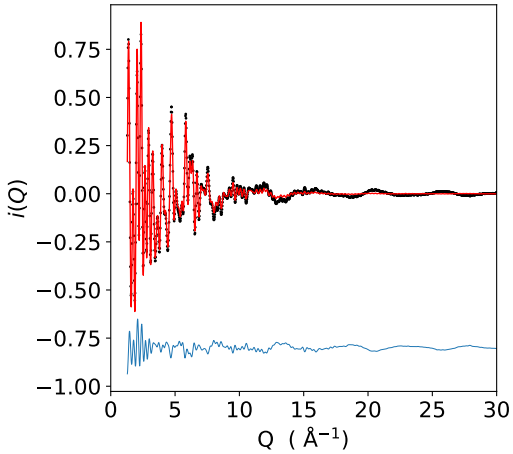

(b) $i(Q)$

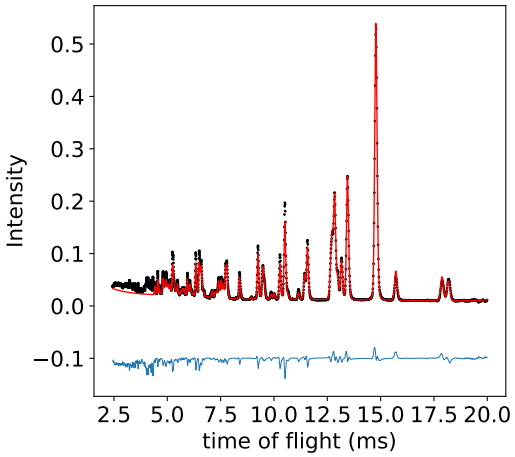

(c) Bragg scattering

Figure 5: Representative RMC fits of (a) pair distribution function, (b) total scattering function, and (c) Bragg pattern, for witherite at room temperature. In each case the black points represent the experimental data, and the red lines represent the RMC fitted functions. The blue lines represent the difference between the experimental and RMC fitted functions.

3. Phase transitions seen in the molecular dynamics simulations

3.1. Simulations starting in the calcite structure

The temperature-dependence of the lattice parameters of both $CaCO_3$ and $BaCO_3$, obtained by MD simulation and starting in the ordered calcite form, are shown in Figure 6. The simulation box gives two orthogonal evaluations of the trigonal a lattice parameter. To highlight the transition to the cubic phase, we actually scale the lattice parameters as $a' = \sqrt{2}a$ and $c' = c/2\sqrt{3}$ to give the values corresponding to those of the cubic phase a lattice parameter. In both cases the transitions to the cubic form is

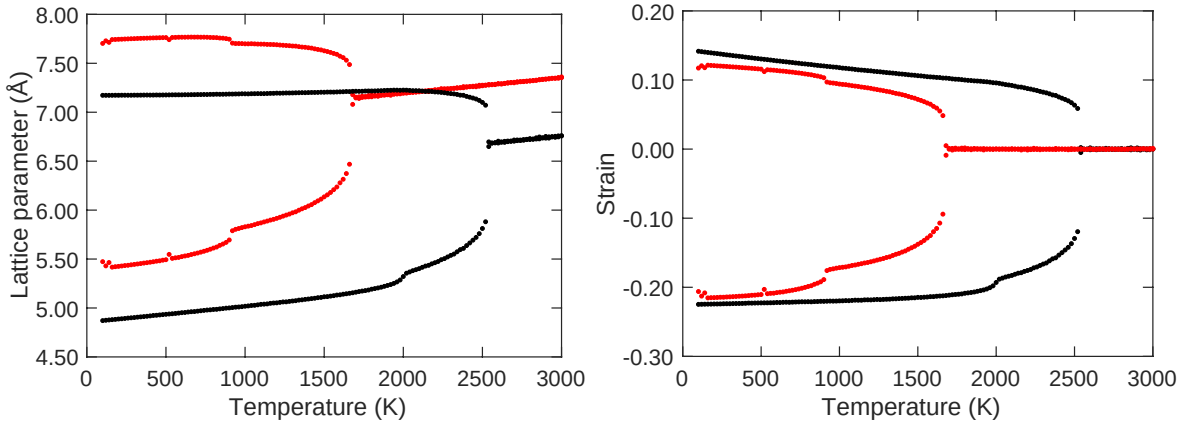

Figure 6: Left: Temperature-dependence of the lattice parameters of $CaCO_3$ (black) and $BaCO_3$ (red) in the calcite form as determined by molecular dynamics simulations. In each case the top curve represents $\sqrt{2}a$ and the lower curve is $c/\sqrt{12}$, the quantities that become the cubic a lattice parameter at high temperature. Right, the corresponding strains obtained by subtracting the extrapolation of the cubic lattice parameter to low tempertures.

very clear – at temperatures of 1665 ± 10 K and 2535 ± 10 K for $BaCO_3$ and $CaCO_3$ respectively – as also are the transitions between the low-temperature ordered phases to the disordered $R\bar{3}m$ phases at temperatures of 905 ± 10 K and 1985 ± 10 K for $BaCO_3$ and $CaCO_3$ respectively. We note that the simulations over-estimate the $R\bar{3}c$–$R\bar{3}m$ transition temperature in calcite by about 60%, and the transition to the cubic phase of $BaCO_3$ is over-estimated by around 30%. However, transition temperatures are very hard to predict from models derived from equilibrium properties only. What is encouraging is that the transition temperatures in $BaCO_3$ are lower than in $CaCO_3$, as expected. What is interesting, however, is that the background thermal expansion around the $R\bar{3}c$–$R\bar{3}m$ transition in both cases is mostly associated with the approach to the transition to the cubic form, and not, as previously assumed [3, 4], due to the ordering associated with the $R\bar{3}c$–$R\bar{3}m$ transition. Figure 6 also shows the strains calculated by comparing the lattice parameters with the extrapolation from the cubic phase, It can be seen that these are extraordinarily large for a phase transition, reaching over 20%.

Configurations from the MD simulation of each phase are shown in Figure 7. The barium and calcium atoms are not shown in these figures in order to make the orientational behaviour of carbonate groups prominent. At low temperature, the carbonate anions in both $BaCO_3$ and $CaCO_3$ are orientationally ordered, although it is clear that the carbonate groups in $BaCO_3$ have spontaneously reoriented to give an ordered structure that is different from both calcite and witherite. As the temperature increases on heating towards the intermediate-temperature phase, the carbonate anions in both cases show growing librational motions about the molecular 3-fold rotational axis and about the orthogonal axes, whilst maintaining the same average orientations. The MD configuration shown in Figure 7b suggests the space group for the intermediate-temperature phase

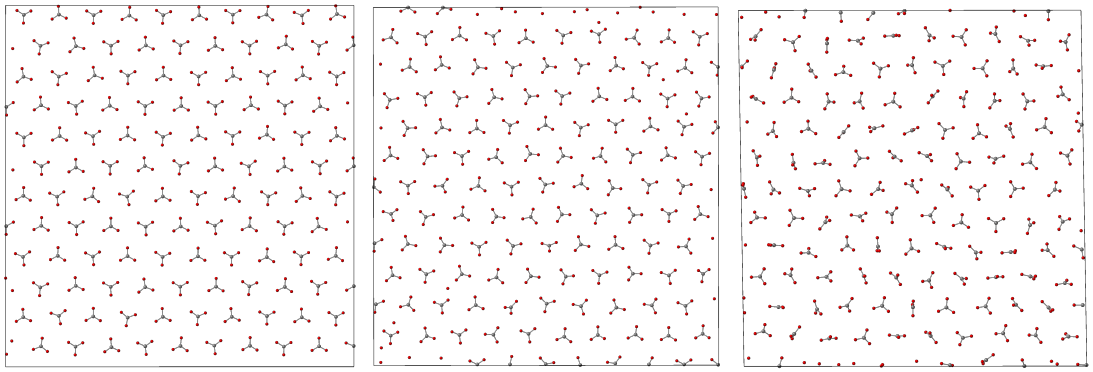

(a) $BaCO_3$, 300 K (b) $BaCO_3$, 1000 K (c) $BaCO_3$, 1700 K

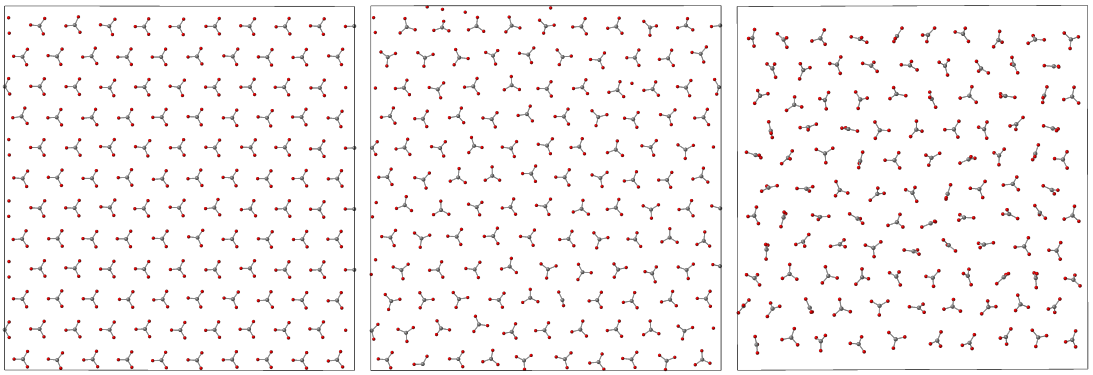

(d) $CaCO_3$, 300 K (e) $CaCO_3$, 2000 K (f) $CaCO_3$, 2600 K

Figure 7: Representative configurations from the MD simulations of $BaCO_3$ (top row) and $CaCO_3$ (bottom row) viewing from the trigonal [001] direction. the alkali metal atoms are excluded from these figures for clarity.

of $BaCO_3$ is $R\bar{3}m$. In Figures 7c and 7f, there are no orientation pattern for carbonate ions, indicating they lose preferred orientations in the cubic phases.

The orientational disorder of the carbonate groups can be seen in the distribution of C–O bond orientations. Figure 8 shows how the distribution of C–O bonds in the MD simulations of $CaCO_3$ evolves with increasing temperature. The distribution broadens on heating and it vanishes in the intermediate temperature phase as shown in 8f. This indicates the C–O bonds in $CaCO_3$ have a preferred orientation along [100] in the low temperature phase. The C–O bonds become more widely spread around [100] with increasing temperature. At intermediate temperatures, the orientational distribution becomes nearly uniform around the equator line with large spread of librations out of this plane.

A similar trend exists in $BaCO_3$, albeit with different orientations of the carbonate molecular ion as noted above, and for which the C–O bond orientation distribution is shown in Figure 9. At 200 K, there are 2 preferred orientations i.e. two concentrated bright dots at the equator lie viewing from the [100] direction. As the temperature increases to 1000 K, shown in Figure 9a to 9d, the C–O orientation becomes more

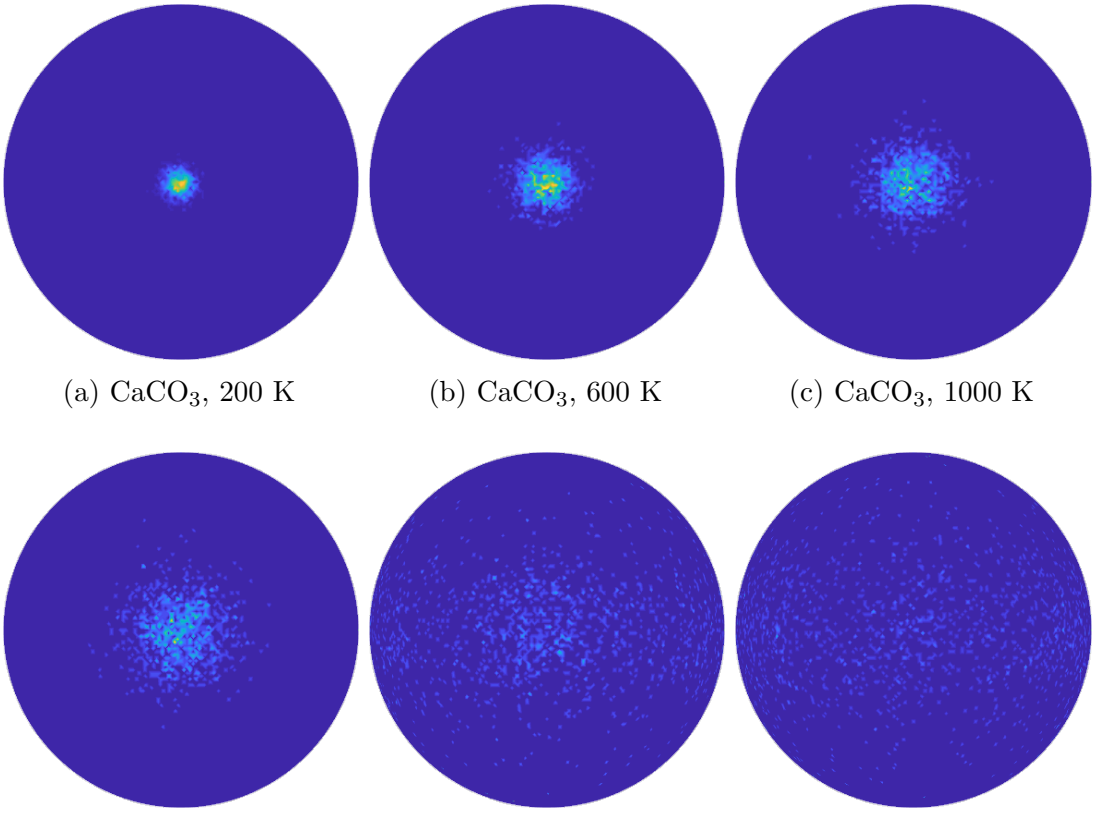

(a) $CaCO_3$, 200 K (b) $CaCO_3$, 600 K (c) $CaCO_3$, 1000 K

(d) $CaCO_3$, 1400 K (e) $CaCO_3$, 2000 K (f) $CaCO_3$, 2200 K

Figure 8: Orthographic projections of the C–O bond orientation distributions for $CaCO_3$ at different temperatures from MD simulations, viewed along the [100] direction. Yellow represents orientations of high probability, whereas while dark blue represents orientations with low probability.

widely spread while the two preferred orientations are still distinguishable (brighter than other solid angles). At the intermediate-temperature phase, as shown in Figure 9e and Figure 9f, the C–O orientation become more evenly spread around the equator and more progressively spread towards the poles.

The C–O bond orientation distribution plots from molecular dynamics simulations suggest that in both $CaCO_3$ and $BaCO_3$ the carbonate ions are orientationally ordered at the low temperature phases. Their rotational and librational vibration amplitudes increase with increasing temperatures resulting in a larger spread of C–O bond orientation distribution. In the intermediate-temperature phase, full disorder with respect to rotation about the threefold axis is achieved and libration out of the molecular plane increases, before the orientations of the carbonate ions become fully disordered at the cubic phase.

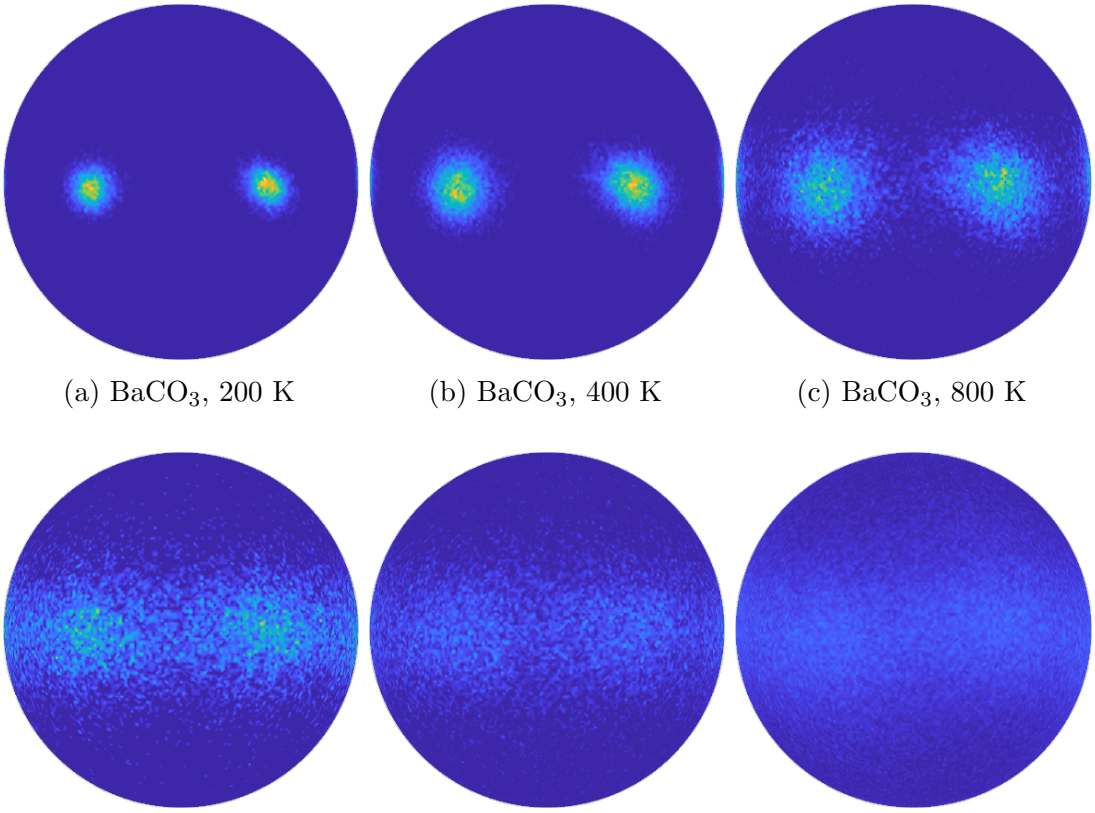

(a) $BaCO_3$, 200 K (b) $BaCO_3$, 400 K (c) $BaCO_3$, 800 K

(d) $BaCO_3$, 1000 K (e) $BaCO_3$, 1200 K (f) $BaCO_3$, 1600 K

Figure 9: Orthographic projections of the C–O bond orientation distributions for $BaCO_3$ at different temperatures from MD simulations, viewed along the [100] direction. The colour scheme is described in the caption to Figure 8.

3.2. Simulations starting in the witherite structure

We also performed simulations of $BaCO_3$ starting in the witherite phase. Over the time scale of the simulations the structure will retain the basic layout of the sites for the Ba and C atoms, but will allow reorientations of the CO_3 groups as seen in the simulations of $BaCO_3$ starting in the calcite structure.

The simulated lattice parameters are shown in Figure 10 and compared with the experimental values derived from Table 1. In Figure 10 we make use of the fact that the atomic structure of the witherite (aragonite) phase has the Ba atoms in an approximate hexagonal close-packed arrangement, with the C atoms in the corresponding octahedral sites to give a structure that is derived from the ideal type structure of NiAs (Strukturbericht type $B8_1$). On this basis, the a lattice parameter of the orthorhombic phase will correspond to that of the hexagonal phase, and the b lattice parameter, representing an orthogonal direction will correspond to a distance equal to $\sqrt{3}$ times the hexagonal a lattice parameter. The c lattice parameter reflects the spacing between the close-packed layers in the hexagonal close-packed arrangement, and will have ideal

value when $c = \sqrt{8/3}a$. Thus in Figure 10 we plot a, $b/\sqrt{3}$ and $c/\sqrt{8/3}$. The hexagonal symmetry is broken by the ordering of the orientations of the carbonate groups, but on heating in the simulation we see a clear phase transition to a hexagonal structure as the carbonate groups develop disorder first with orientations about the molecular 3-fold axis and then as full three-dimensional disorder.

The experimental lattice parameters for the witherite phase, shown in Figure 10, follow the simulated values up to the point of the transition to the rhombohedral phase. Given the structural similarities between the Strukturbericht type B_1 and $B8_1$ structures, the energies of the two phases will be very similar. In general phase transitions or metastable co-existence of these types of structures is common. It is therefore not surprising that as the experimental witherite phase begins to disorder, it switches structure to a distorted B_1 type structure rather than following the behaviour seen in the simulation. What is interesting from Figure 10 is the close correspondence between the simulated and experimental lattice parameters. The experimental coefficients of the thermal expansion at higher temperatures in the witherite phase are $\alpha_a = 5 \times 10^{-6}$ K^{-1}, $\alpha_b = 13 \times 10^{-6}$ K^{-1}, and $\alpha_c = 82 \times 10^{-6}$ K^{-1}. The relatively large experimental value of α_c can therefore be understood in terms of the onset of three-dimensional disorder, and the smaller temperature variation of the a and b lattice parameters can be understood in terms of the convergence of these quantities in the simulated transition to a hexagonal phase.

4. Results from the Reverse Monte Carlo analysis of $BaCO_3$

4.1. Atomic structures

Figure 11 show representative layers of the configurations from the RMC analysis, which in the cases of the witherite phase and the intermediate rhombohedral phase are view down the directions perpendicular to the alignment of the molecular 3-fold axes in the crystal structures. In comparison with Figure 7 it will noted there are bond-bending distortions of the carbonate molecular ions here that are not seen in the MD configurations. This is because the carbonate ions are held rigidly fixed in shape in the MD simulations but are clearly allowed to distort in reality and as seen in the RMC simulations.

4.2. Witherite phase

Figure 12a shows the distribution of C–O bond orientations within the RMC configurations for the witherite phase, and the corresponding distribution from the MD simulations is shown in Figure 12b. The distributions for the RMC models for the two rhombohedral-phase starting points are shown in Figures 12c and 12d. As compared with the MD (Figure 9), the distribution shows more motion of the bonds corresponding to rotations about axes perpendicular to the carbonate three-fold rotation axis. This is consistent with the extraordinary large values of the atomic displacement parameter U_{33}

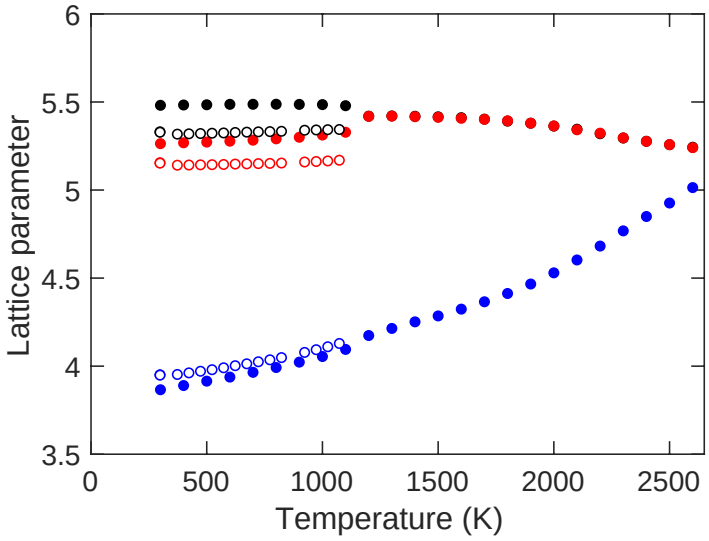

Figure 10: Temperature-dependence of the lattice parameters of $BaCO_3$ in the orthorhombic witherite form obtained by MD simulation (filled circles) and from Rietveld refinement of the neutron powder diffraction data (open circles). The black points are a, red points are $b/\sqrt{3}$, and blue points are $c/\sqrt{8/3}$. The scaling is explained in the text, and is chosen so that the scaled a and b lattice parameters will come together in value with a phase transition from the orthorhombic to disordered hexagonal structure, and the scaled c lattice parameter will become closer in value as the disordered hexagonal phase approaches the ideal close-packed structure.

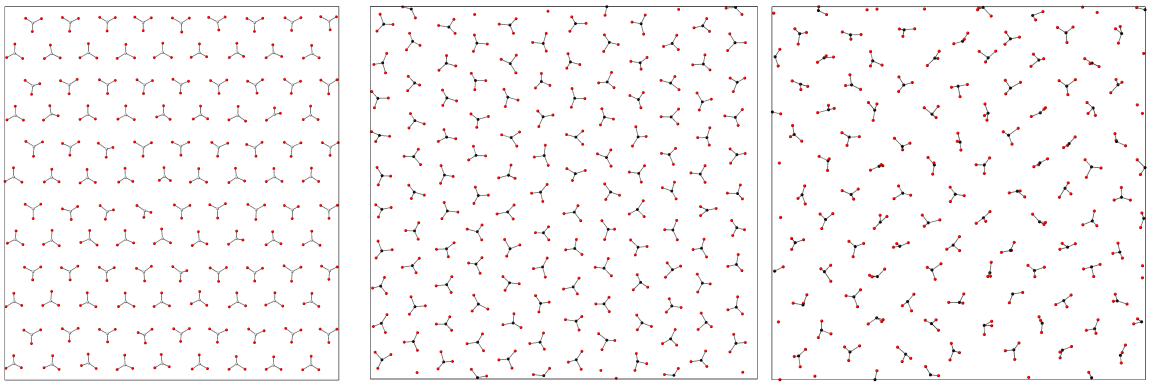

(a) $BaCO_3$, 300 K (b) $BaCO_3$, 1203 K (c) $BaCO_3$, 1273 K

Figure 11: Representative carbonate atomic layers from the RMC configurations of $BaCO_3$ viewing from the crystallographic [001] directions in each case. Ba atoms are excluded from these figures for clarity.

values given in Table 3, and is fully consistent with the phase behaviour discussed earlier as revealed by the MD simulations.

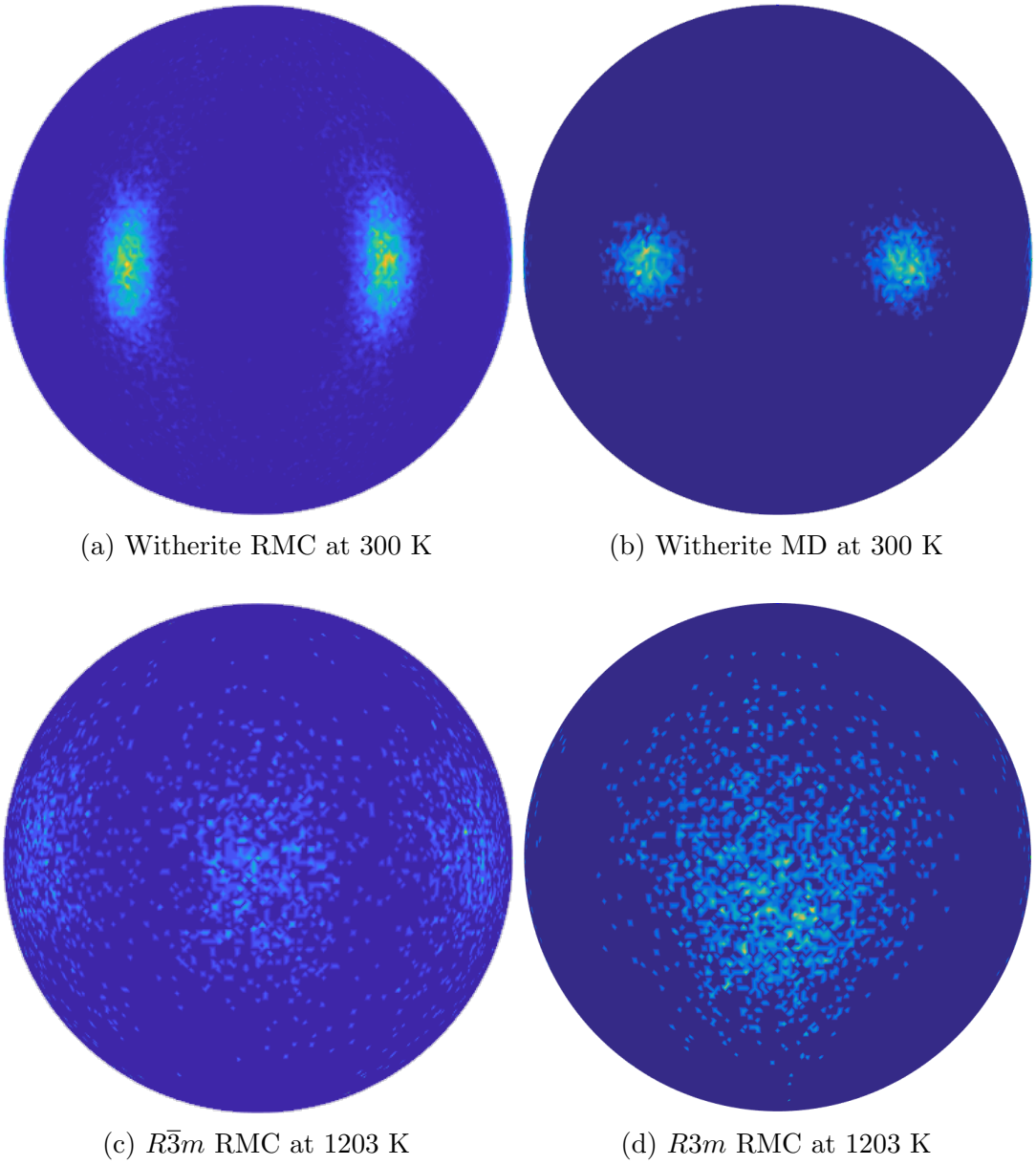

(a) Witherite RMC at 300 K (b) Witherite MD at 300 K

(c) $R\bar{3}m$ RMC at 1203 K (d) $R3m$ RMC at 1203 K

Figure 12: Orthographic projections of the C–O bond orientation distributions for $BaCO_3$ in the witherite phase at 300 °C from the RMC and MD simulations, and for the rhombohedral phases with space groups $R\bar{3}m$ and $R3m$ at 930 °C, each viewed along the [100] direction. The colour scheme is described in the caption to Figure 8.

4.3. Rhombohedral phase

Although in our previous discussion on the Rietveld analysis we remarked that we believe that the rhombohedral phase is more likely to have the disordered $R\bar{3}m$ structure than that with space group $R3m$, we explored using both the $R\bar{3}m$ and $R3m$ structures as the starting configurations for the RMC analysis of this phase. In fact we found that both give similar quality fits to the three sets of data, and the structures remained the

same throughout the RMC simulation. Thus RMC is not giving us a preference for one structure over the other.

Figure 12c shows the C–O bond orientation distribution for the $R\bar{3}m$ phase, and that for the $R3m$ phase is shown in Figure 12d. Similar to the RMC and MD results shown in Figures 12a and 12b for the room-temperature witherite phase, the vertical libration is more prominent than the horizontal rotation movement. This is consistent with the atomic displacements parameters obtained from Rietveld refinement as show in Tables 3 and 4; although the values of U_{11} and U_{22} increase dramatically in the rhombohedral phase, they remain smaller than the value of U_{33}.

4.4. Cubic phase

The various partial pair distribution functions $g(r)$ from both RMC and MD configurations for cubic $BaCO_3$ are shown in Figure 13. The overall match is good, albeit with a very slight difference in length scale. The $g(r)$ functions for the Ba–Ba, Ba–C and C–C pairs reflect the simple rocksalt structure. The more interesting functions are those involving the oxygen atoms, because these will reflect the degree of disorder, and here the agreement between MD and RMC is considered to be good. Small differences will be a reflection of some small differences in bond orientational distribution function described next.

In the cubic phase of $BaCO_3$, and theoretically of $CaCO_3$ also, the carbonate groups (molecular point group symmetry $3/m$) occupy sites of the full octahedral symmetry (point group $m\bar{3}m$). The lower symmetry of the molecular anion implies that there must be orientational disorder. Such cases of orientationally disordered crystals are common; examples are KCN [27, 28], and CBr_4 and SF_6 [29]. It is common to characterise the atomic structure in terms of the orientational distribution of the component bonds of the molecules, which in this case means the angular distribution of the C–O bonds. It is then common to represent this as a distribution function in terms of polar angles $\Omega = (\theta, \phi)$, defined mathematically as an expansion in terms of the Kubic harmonics, which are formed as symmetry-adapted combinations of spherical harmonics, and are defined in the Appendix for convenience [29, 30]. The bond orientational distribution function is thus defined as

$$P(\Omega) = \frac{1}{4\pi} \sum_{\ell} c_\ell K_\ell(\Omega) \tag{3}$$

In diffraction experiments the coefficients c_ℓ can be fit in a structure refinement [29]. On the other hand, in a simulation that gives a configuration of atoms we can obtain the values of the coefficients as $c_\ell = \langle K_\ell \rangle$, a result that follows directly from the orthornormality of the functions $K_\ell(\Omega)$. The average is performed over all bonds in the atomic configuration, and for higher accuracy (as done here) can also be averaged over several independent configurations. Values of c_ℓ for the distribution of C–O bonds in the cubic phase of $BaCO_3$ as obtained from both RMC and MD are given in Table 5, together with corresponding values for calcite from MD.

Table 5: Values of the coefficients c_ℓ in the expansion of the C–O bond orientational distribution function $P(\Omega)$ as defined by equation 3. These values were obtained by averaging over several atomic configurations as described in the text. Note that $c_0 = 1$.

	T (K)	c_4	c_6	c_8	c_{10}
$BaCO_3$ RMC	1203	−0.117	0.019	0.010	−0.005
$BaCO_3$ MD	1660	0.1745	−0.042	0.057	−0.006
$BaCO_3$ MD	3000	0.028	−0.009	−0.004	0.007
$CaCO_3$ MD	2520	0.171	−0.013	0.031	0.004
$CaCO_3$ MD	3000	0.0497	−0.028	−0.016	−0.005

Figure 14 shows the C–O bond orientational distribution function for cubic $BaCO_3$ calculated from the RMC configurations. We display both the bond distribution function calculated point-by-point from the histogram of bond angles, and as calculated from equation 3. The value $P(\Omega) = 1/4\pi$ corresponds to a uniform distribution function. It is seen that is some preference for alignment away from the $\langle 100 \rangle$ directions, but only of the order of just over 10% variation away from the uniform distribution. Other orientationally-disordered crystals can show much more structure in the bond orientational distribution function.[29]

Figure 15 shows the C–O bond orientational distribution functions for cubic $BaCO_3$ and $CaCO_3$ calculated from the MD configurations. These distributions are more uniform than in the RMC configurations, but the phase transitions are at higher temperatures and so these distributions represent correspondingly higher temperatures. In fact the distributions become more uniform on heating, since over the temperature range 1500–3000 K the value of the coefficient c_4 for cubic $BaCO_3$ falls by about one half. The distributions in both $BaCO_3$ and $CaCO_3$ differ from the RMC in that they show slight preferences for orientations along the $\langle 100 \rangle$ directions rather than away from these directions, but the effects are actually very slight.

5. Discussion and conclusion

The key objective of this paper was to identify the orientational disorder in the cubic phase of $BaCO_3$, which we have shown by both RMC and MD to be almost completely uniform. Given the shape of the CO_3 molecular anion, it is not surprising that this might be so. We see from lower-temperature MD data and earlier crystallographic data on $CaCO_3$ that although the C–O bond has a preference to point along symmetry directions in the hexagonal basal plane, it has a large growth in out-of-plane orientations on heating.

The existence of the cubic phase of $BaCO_3$ that is reflected also in the MD simulations of both systems leads to a new interpretation of the observed phase transition in $CaCO_3$. Previously it was assumed that the main phase transition was from space groups $R\bar{3}c$ to $R\bar{3}m$ on heating, with the onset of orientational disorder about the 3-fold axis leading to halving of the crystallographic repeat distance parallel to the 3-fold axis. The onset

of decomposition at the phase transition meant that it was impossible to confirm the existence of the higher-symmetry phase, but loss of certain Bragg peaks on heating to the transition are only consistent with this explanation. What was previously unexplained was the fact that on heating towards the phase transition the largest orientational fluctuations were associated with tilting of the 3-fold axis away from the plane normal rather than about this axis. This is seen also in the MD simulations of the $R\bar{3}c$ in calcite, Figure 8. Furthermore, without data on the lattice parameters for temperatures above the phase transition it was hard to analyse the strains associated with ordering. What emerges from the MD results presented here is that the variation of the lattice parameters with temperature is affected primarily by the spontaneous strains associated with the transition to the cubic phase and not between the two rhombohedral phases. This is a completely new viewpoint on the phase behaviour of the important mineral calcite.

6. Postscript: some personal comments by the corresponding author

The corresponding author (MTD) held his first post-doctoral research position in the Department of Physics at the University of Edinburgh during the time when Roger Cowley was head of department. Edinburgh Physics was an exciting environment at that time. The Condensed Matter group had a large grant covering the activities of all the research-active staff, mostly in the general area of phase transitions. My personal interest was in molecular crystals, working with Stuart Pawley, but from my PhD I had been inspired by the work of Roger, and his supervisor Bill Cochran (also in Edinburgh at the time). Prior to coming to Edinburgh I had studied hard (and bought the resultant book of) the three papers of Roger and Alastair Bruce on phase transitions in the journal Advances in Physics [31, 32, 33]. I have also been helped throughout my career by Roger's analysis of the acoustic modes that accompany ferroelastic phase transitions [34], and have used the measurement of the soft mode in $SrTiO_3$ performed by Roger in collaboration with Bill Buyers and Gerald Dolling [35].

Roger and I were co-authors on just one paper, concerning the ferroelastic phase transition at 755 K in Na_2CO_3 [36], another carbonate material. This transition is a second-order transition between hexagonal and monoclinic space groups. The symmetry change is such that there is a softening of one set of acoustic modes lying for all wave vectors within a plane in reciprocal space. Previously Roger and Andreas Meyer had shown that such a case is very similar to melting in two dimensions [37], and the amazing thing was to indeed see all the Bragg peaks except those with Miller indices of the form (00ℓ) disappear at the phase transition, to be replaced by broad peaks of diffuse scattering [36, 38, 39], fully consistent with the theory [37]. It was characteristic of Roger's modesty that he declined to be co-author on the other papers in the series by Mark Harris, as his postdoctoral assistant, and I. Moreover, Roger showed a lot of interest in our work on the anomalous inelastic scattering of radiation in calcite [40, 41] and the related system $NaNO_3$ [42] carried out by Mark Harris and I, but again never requesting to appear as co-author.

It is fair to say that Roger had become one of my heroes as a young research student, before I subsequently had the privilege to work in his department, and he has remained as such throughout my whole career. And whilst it is said that you should never meet your heroes, because they often disappoint you, this was definitely not the case with Roger.

7. Acknowledgements

We are grateful to the ISIS Neutron and Muon Facility for provision of beam time; award reference is RB810276, and the DOI for the data is 10.5286/ISIS.E.RB810276. GC acknowledges financial support from the China Scholarship Council and Queen Mary University of London. This research made use of two large-scae computing facilities. The first was the Apocrita HPC facility of Queen Mary University of London, supported by QMUL Research-IT, and initially funded by EPSRC grants EP/K000128/1 and EP/K000233/1 (MTD). The second was the EPSRC-funded HPC Midlands Plus (EP/P020232/1) Tier-2 system, which we accessed as members of the project consortium (MTD). Figures showing crystal and configuration structures were prepared using the CrystalMaker software [43].

8. References

[1] R Srinivasan. The thermal expansion of calcite from room temperature up to 400°C. *Proceedings of the Indian Academy of Sciences - Section A*, 42:81–85, 1955.

[2] S A Markgraf and R J Reeder. High-temperature structure refinements of calcite and magnesite. *American Mineralogist*, 70:590–600, 1985.

[3] M T Dove and B M Powell. Neutron diffraction study of the tricritical orientational order/disorder phase transition in calcite at 1260 K. *Physics and Chemistry of Minerals*, 16:1–5, 1989.

[4] Martin T Dove, Ian P Swainson, Brian M Powell, and Donald C Tennant. Neutron powder diffraction study of the orientational order–disorder phase transition in calcite, $CaCO_3$. *Physics and Chemistry of Minerals*, 32:493–503, 2005.

[5] J P R de Villiers. Crystal structures of aragonite, strontianite, and witherite. *American Mineralogist*, 56:758–767, 1971.

[6] Sytle M Antao and Ishmael Hassan. $BaCO_3$: high-temperature crystal structures and the $Pmcn \rightarrow R3m$ phase transition at 811 °C. *Physics and Chemistry of Minerals*, 34:573–580, 2007.

[7] S M Antao and I Hassan. The orthorhombic structure of $CaCO_3$, $SrCO_3$, $PbCO_3$ and $BaCO_3$: linear structural trends. *The Canadian Mineralogist*, 47:1245–1255, 2009.

[8] Y Ye, J R Smyth, and P Boni. Crystal structure and thermal expansion of aragonite-group carbonates by single-crystal x-ray diffraction. *American Mineralogist*, 97:707–712, 2012.

[9] K O Strömme. On the crystal structures of the high-temperature forms of strontium and barium carbonate and structurally related compounds. *Acta Chemica Scandinavica*, 29a:105–110, 1975.

[10] Ilian T Todorov, William Smith, Kostya Trachenko, and Martin T Dove. DL_POLY_3: new dimensions in molecular dynamics simulations via massive parallelism. *Journal of Materials Chemistry*, 16:1911–8, 2006.

[11] T D Archer, S E A Birse, M T Dove, S A T Redfern, J D Gale, and R T Cygan. An interatomic potential model for carbonates allowing for polarization effects. *Physics and Chemistry of Minerals*, 30:416–424, 2003.

[12] Paolo Raiteri, Julian D Gale, David Quigley, and P Mark Rodger. Derivation of an Accurate Force-Field for Simulating the Growth of Calcium Carbonate from Aqueous Solution: A New Model for the Calcite—Water Interface. *The Journal of Physical Chemistry C*, 114:5997–6010, 2010.

[13] Martin T Dove and Gary Rigg. RMCgui: a new interface for the workflow associated with running Reverse Monte Carlo simulations. *Journal of Physics: Condensed Matter*, 25:454222–9, 2013.

[14] M Parrinello and A Rahman. Crystal Structure and Pair Potentials: A Molecular-Dynamics Study. *Physical Review Letters*, 45(14):1196–1199, October 1980.

[15] Simone Melchionna, Giovanni Ciccotti, and Brad Lee Holian. Hoover NPTdynamics for systems varying in shape and size. *Molecular Physics*, 78(3):533–544, August 2006.

[16] Shuichi Nosé. A unified formulation of the constant temperature molecular dynamics methods. *The Journal of Chemical Physics*, 81(1):511–10, 1984.

[17] William G Hoover. Canonical dynamics: Equilibrium phase-space distributions. *Physical Review A*, 31(3):1695–1697, March 1985.

[18] Alex C Hannon. Results on disordered materials from the GEneral Materials diffractometer, GEM, at ISIS. *Nuclear Instruments and Methods in Physics Research Section A: Accelerators, Spectrometers, Detectors and Associated Equipment*, 551:88–107, 2005.

[19] O Arnold, J C Bilheux, J M Borreguero, A Buts, S I Campbell, L Chapon, M Doucet, N Draper, R Ferraz Leal, M A Gigg, V E Lynch, A Markvardsen, D J Mikkelson, R L Mikkelson, R Miller, K Palmen, P Parker, G Passos, T G Perring, P F Peterson, S Ren, M A Reuter, A T Savici, J W Taylor, R J Taylor, R Tolchenov, W Zhou, and J Zikovsky. Mantid—Data analysis and visualization package for neutron scattering and μ SR experiments. *Nuclear Inst. and Methods in Physics Research, A*, 764(C):156–166, 2014.

[20] Alan K Soper. GudrunN and GudrunX : programs for correcting raw neutron and X-ray diffraction data to differential scattering cross section. Technical Report RAL-TR-2011-013, Rutherford Appleton Laboratory, 2011.

[21] David A Keen. A comparison of various commonly used correlation functions for describing total scattering. *Journal of Applied Crystallography*, 34:172–177, 2001.

[22] A C Larson and R B Von Dreele. General Structure Analysis System (GSAS). Technical Report LAUR 86-748, Los Alamos National Laboratory, 2004.

[23] Brian H Toby. EXPGUI, a graphical user interface for GSAS. *Journal of Applied Crystallography*, 34:210–213, 2001.

[24] Brian H Toby and Robert B Von Dreele. GSAS-II: the genesis of a modern open-source all purpose crystallography software package. *Journal of Applied Crystallography*, 46:544–549, 2013.

[25] Matthew G Tucker, David A Keen, Martin T Dove, Andrew L Goodwin, and Qun Hui. RMCProfile: reverse Monte Carlo for polycrystalline materials. *Journal of Physics: Condensed Matter*, 19:335218–16, 2007.

[26] Wojciech A Sławiński. Calculation of pair distribution functions for multiphase systems. *Journal of Applied Crystallography*, 51(3):919–923, June 2018.

[27] JM Rowe, JJ Rush, and E Prince. Neutron diffraction study of the structure and phase transitions of alkali cyanide crystals. *The Journal of Chemical Physics*, 66:5147–5149, 1977.

[28] J M Rowe, J J Rush, N J Chesser, K H Michel, and J Naudts. Nature of the Phase Transition in KCN at 168 K. *Physical Review Letters*, 40:455–458, 1978.

[29] G Dolling, B M Powell, and V F Sears. Neutron diffraction study of the plastic phases of polycrystalline SF_6 and CBr_4. *Molecular Physics*, 37:1859–1883, 1979.

[30] W R Fehlner and S H Vosko. A product representation for cubic harmonics and special directions for the determination of the Fermi surface and related properties. *Canadian Journal of Physics*, 54:2159–2169, 1976.

[31] R. A. Cowley. Structural phase transitions I. Landau theory. *Advances in Physics*, 29:1–110, 1980.

[32] Alastair D. Bruce. Structural phase transitions. II. Static critical behaviour. *Advances in Physics*, 29:111–217, 1980.

[33] Alastair D. Bruce and R. A. Cowley. Structural phase transitions III. Critical dynamics and quasi-elastic scattering. *Advances in Physics*, 29:219–321, 1980.

[34] R. A. Cowley. Acoustic phonon instabilities and structural phase transitions. *Phys. Rev. B*, 13:4877–4885, 1976.

[35] R.A. Cowley, W. J. L. Buyers, and G. Dolling. Relationship of normal modes of vibration of strontium titanate and its antiferroelectric phase transition at 110°K. *Solid State Communications*, 7:181–184, 1969.

[36] M. J. Harris, R. A. Cowley, Ian P. Swainson, and Martin T. Dove. Observation of lattice melting at the ferroelastic phase transition in Na_2CO_3. *Phys. Rev. Lett.*, 71:2939–2942, 1993.

[37] A P Mayer and R A Cowley. The continuous melting transition of a three-dimensional crystal at a planar elastic instability. *Journal of Physics C: Solid State Physics*, 21:4827–4834, 1988.

[38] I P Swainson, M T Dove, and M J Harris. Neutron powder diffraction study of the ferroelastic phase transition and lattice melting in sodium carbonate, Na_2CO_3. *Journal of Physics: Condensed Matter*, 7:4395–4417, 1995.

[39] M. J. Harris, M. T. Dove, and K. W. Godfrey. Observation of lattice melting in a single crystal: The ferroelastic phase transition in Na_2CO_3. *Phys. Rev. B*, 51:6758–6760, 1995.

[40] M T Dove, M E Hagen, M J Harris, B M Powell, U Steigenberger, and B Winkler. Anomalous inelastic neutron scattering from calcite. *Journal of Physics: Condensed Matter*, 4:2761–2774, 1992.

[41] M J Harris, M T Dove, I P Swainson, and M E Hagen. Anomalous dynamical effects in calcite. *Journal of Physics: Condensed Matter*, 10:L423–L429, 1998.

[42] M J Harris, M E Hagen, M T Dove, and I P Swainson. Inelastic neutron scattering, phonon softening, and the phase transition in sodium nitrate. *Journal of Physics: Condensed Matter*, 10:6851–6861, 1998.

[43] David C Palmer. Visualization and analysis of crystal structures using CrystalMaker software. *Zeitschrift für Kristallographie - Crystalline Materials*, 230(9-10):559–572, August 2015.

Appendix A. Definition of the Kubic harmonic functions

We reproduce here the first five Kubic harmonics K_ℓ in Cartesian, using the definitions $Q = x^4 + y^4 + z^4$ and $S = x^2y^2z^2$, where $x = \sin\theta\cos\phi$, $y = \sin\theta\sin\phi$ and $z = \cos\theta$ [29, 30].

$$K_0 = 1$$

$$K_4 = \frac{\sqrt{21}}{4}(5Q - 3)$$

$$K_6 = \frac{\sqrt{13}}{8\sqrt{2}}(462S + 21Q - 17)$$

$$K_8 = \frac{\sqrt{561}}{32}(65Q^2 - 208S - 94Q + 33)$$

$$K_{10} = \frac{\sqrt{455}}{64\sqrt{2}}(7106QS + 187Q^2 - 3190S - 264Q + 85)$$

Note that terms with odd values of ℓ are absent due to symmetry, as also is the term for $\ell = 2$.

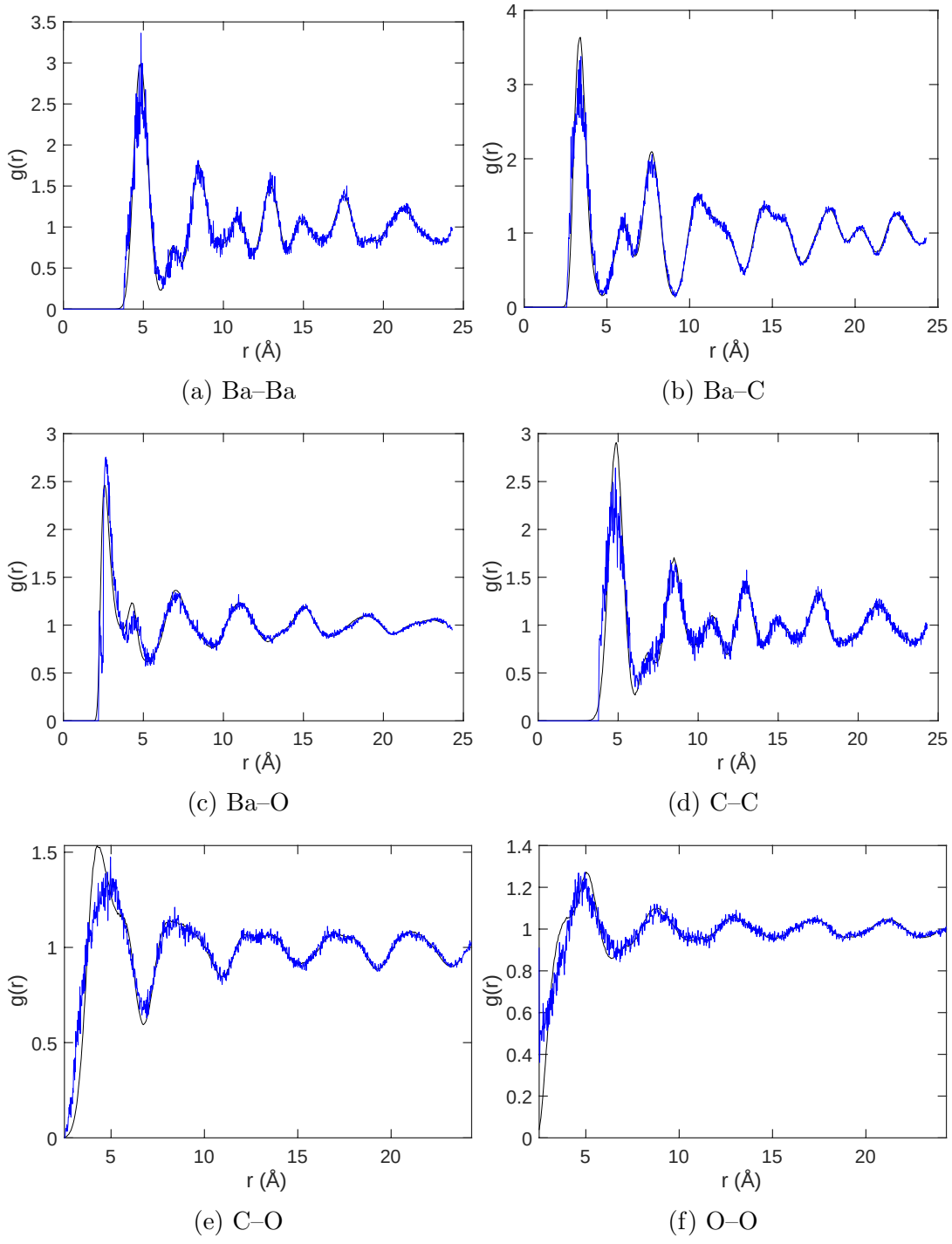

(a) Ba–Ba (b) Ba–C

(c) Ba–O (d) C–C

(e) C–O (f) O–O

Figure 13: Partial pair distribution functions $g_{mn}(r)$ for cubic $BaCO_3$ from RMC (blue lines) and MD (black curves) for each of the atomic pairs. Note that we do not include the low-r part for the C–O and O–O functions because the peaks in the MD simulations are δ-functions since we used rigid carbonate molecular anions. Due to the simulation transition temperature being higher than experiment, the PDFs for experiment are at 1273 K and for the simulation at 2600 K. A small rescaling of the values of r for the MD data was applied to bring the peaks into best registry, accounting for imperfections in the interatomic potentials and the effects of thermal expansion.

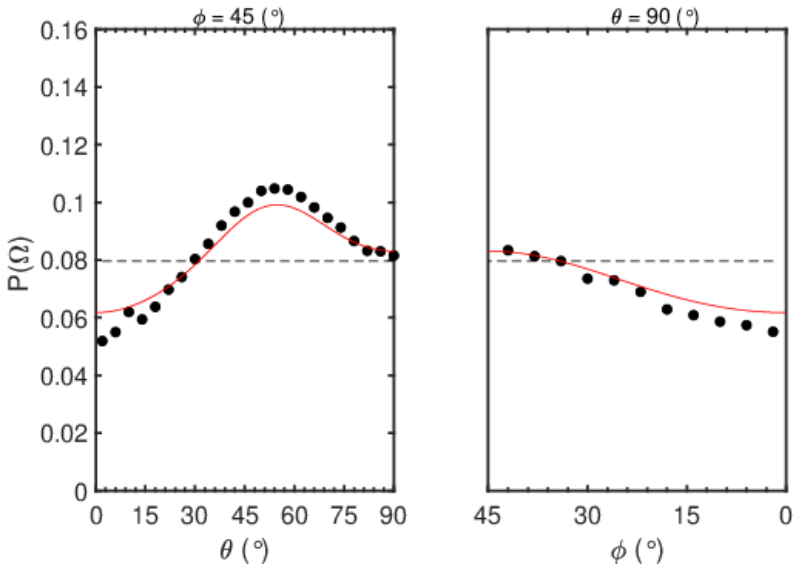

Figure 14: C–O bond orientational distribution function for cubic $BaCO_3$ from RMC. The points are histograms of the actual distribution in the RMC configurations, and the red line is calculated from the Kubic harmonic functions, equation 3. The horizontal dashed line at $P = 1/4\pi$ is the value for a uniform distribution.

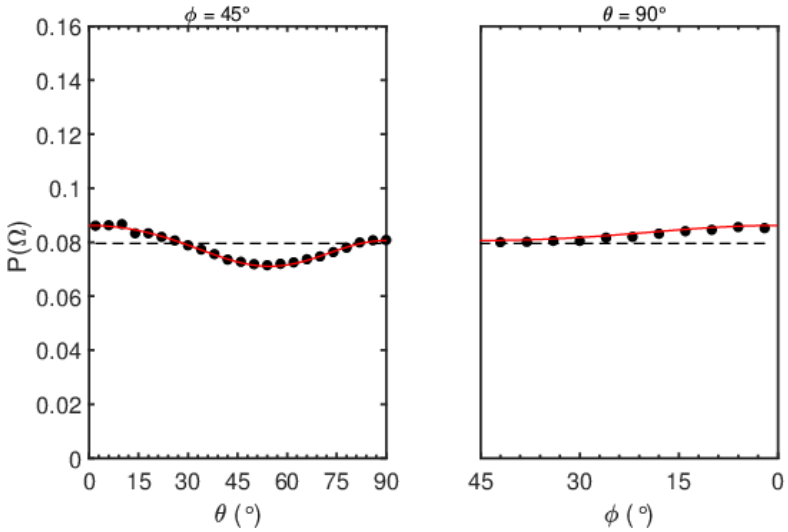

(a) $CaCO_3$

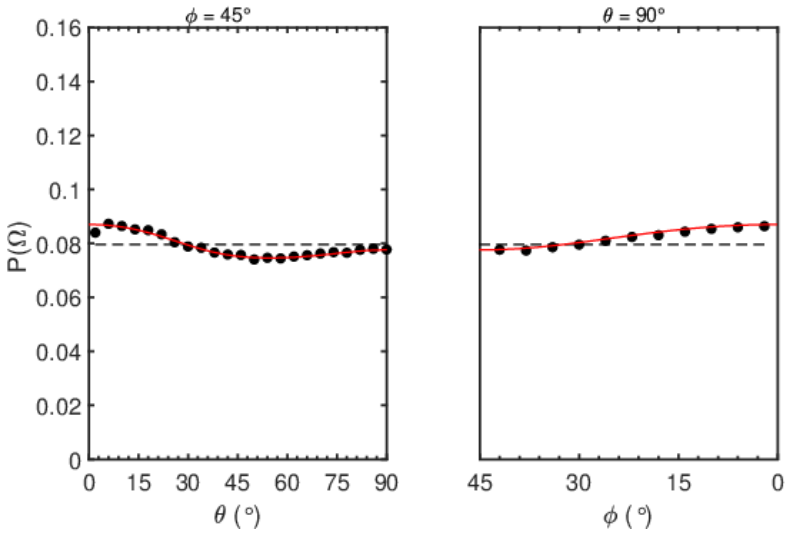

(b) $BaCO_3$

Figure 15: C–O bond orientational distribution function for cubic $BaCO_3$ and $CaCO_3$ from MD simulations. The points are histograms of the actual distribution in the RMC configurations, and the red line is calculated from the Kubic harmonic functions, equation 3. The horizontal dashed line at $P = 1/4\pi$ is the value for a uniform distribution.